Aerosol Size Distribution and New Particle Formation in High Mountain Environments: A Comparative Study at Monte Cimone and Jungfraujoch GAW Stations

Martina Mazzini[1,2], Diego Aliaga[3,4], Janne Lamphilati[3], Martin Gysel-Beer[5], Benjamin Tobias Brem[5], Robin Lewis Modini[5], Dominic Heslin-Rees[4], Tareq Hussein[3,6], Marco Zanatta[1], Paolo Cristofanelli[1], Federico Bianchi[3], Markku Kulmala[3], and Angela Marinoni[1]

[1]National Research Council of Italy, Institute of Atmospheric Sciences and Climate (CNR-ISAC), 40129 Bologna, Italy
[2]Department of Pure and Applied Sciences (DiSPeA), Faculty of Earth Science, University of Urbino, 61029 Urbino, Italy
[3]Institute for Atmospheric and Earth System Research/Physics, Faculty of Science, University of Helsinki, Helsinki, 00014 Finland
[4]Department of Environmental Science (ACES), University of Stockholm, Stockholm, 114 18, Sweden
[5]Laboratory of Atmospheric Chemistry, Paul Scherrer Institute, Villigen, Switzerland
[6]Environmental and Atmospheric Research Laboratory (EARL), Department of Physics, School of Science, The University of Jordan, Amman 11942, Jordan

Correspondence: Martina Mazzini (m.mazzini@isac.cnr.it)

Abstract. Aerosol particles modulate Earth's radiation budget and cloud microphysics, yet the processes that control their formation in the free troposphere (FT) are still poorly understood. Monitoring aerosol size distributions and new particle formation (NPF) in this region is crucial to understanding secondary aerosol production, growth dynamics, and their broader climatic implications. We analysed approximately two years of size-resolved aerosol and ion measurements from two high-altitude GAW/ACTRIS stations, Monte Cimone (2165 m a.s.l., GAW ID: CMN) and Jungfraujoch (3580 m a.s.l., GAW ID: JFJ), to characterise aerosol populations and the frequency-intensity of new particle formation in the European free troposphere. Three different NPF classification methods were applied and compared to assess event frequency and characteristics at both sites. Particles larger than 25 nm exhibited marked seasonal variability, largely influenced by boundary layer dynamics. In contrast, the overall abundance of freshly nucleated particles remained relatively stable throughout the year, being significantly perturbed only during NPF events. Interestingly, despite a consistently higher background of freshly nucleated particles at JFJ, NPF events were more frequent and more intense at CMN. CMN displayed higher particle formation and growth rates, likely due to its lower elevation and proximity to the polluted Po Valley, leading to a stronger influence from boundary layer emissions. In contrast, JFJ, located in a cleaner high-Alpine environment, experienced fewer anthropogenic influences and less intense nucleation events. At both sites, a low condensation sink before NPF onset was identified as a critical factor that favours nucleation.

1 Introduction

Aerosol particles impact air quality, human health, and climate (Fuzzi et al., 2015; WHO, 2021; IPCC, 2021). They influence Earth's radiation budget by scattering and absorbing sunlight, causing cooling or warming depending on their nature and composition. Additionally, aerosols act as cloud condensation nuclei (CCN), altering cloud properties and precipitation, which impact Earth's energy balance and climate (Rosenfeld et al., 2014; Seinfeld et al., 2016). Aerosol-cloud interactions are strongly influenced by particle number concentration, size distribution, and chemical composition, making their understanding essential for improving climate models and predicting future climate trends (IPCC, 2021). Despite its importance, new particle formation (NPF), a major source of atmospheric aerosols, remains poorly understood. NPF begins when low-volatility vapors from gas-phase reactions produce molecular clusters, which subsequently grow via condensation and coagulation into nanometer-sized particles (Kulmala et al., 2006; Lee et al., 2019). Sulfuric acid and organic compounds play a key role in NPF, which contributes 50–80% of CCN at 0.5% supersaturation in the lower troposphere, and up to 90% in the free troposphere (Zhao et al., 2024). NPF plays a major role in shaping particle number concentrations in the upper troposphere (Merikanto et al., 2009; Dunne et al., 2016), but uncertainties in model parameterisations still lead to large variability among simulations (Sellegri et al., 2019). The frequency of NPF events vary widely across locations (Laj et al., 2020; Bousiotis et al., 2021), depending on precursor gas availability and background aerosol concentrations (Dada et al., 2017). The respective contributions of ion-mediated versus neutral nucleation remain debated (Bianchi et al., 2016), further complicating our understanding of these processes. Given these knowledge gaps, characterising NPF across different atmospheric regimes, from polluted to pristine regions, is essential. Most studies on particle number size distribution (PNSD) have focused on the planetary boundary layer (PBL), where anthropogenic emissions dominate (Peng et al., 2014; Kerminen et al., 2018; Dinoi et al., 2023). However, research on particles in the FT remains limited (Bianchi et al., 2016; Sellegri et al., 2019), despite its importance in understanding long-range transport and aerosol-climate interactions. Aerosols transported into the FT have longer atmospheric lifetimes and can influence larger spatial areas. Although high-altitude sites are considered representative of the FT, they may experience significant injections of air from the PBL perturbing the natural population of precursor gases and altering or driving NPF dynamics (Bianchi et al., 2022). Long-term aerosol measurements at high-altitude sites such as Monte Cimone (CMN) and Jungfraujoch (JFJ) provide high-quality data on aerosol particle concentration and size distribution in the atmosphere. Their strategic locations allow observation of aerosol properties with minimal local emissions, offering insights into broader atmospheric processes. However, these stations do not always reflect pure FT conditions as valley winds and topographic effects transport air from lower altitudes, influencing measurements (Collaud Coen et al., 2018). During summer, thermal convection can carry air masses from the Po Valley, the Tyrrhenian Sea, or the Swiss Plateau to these sites, enhancing diurnal variability in aerosol concentrations (Lugauer et al., 2000; Marinoni et al., 2008; Cristofanelli et al., 2018). The PBL-FT interface offers favorable conditions for NPF, as aerosol precursors mix with clean, cold air under enhanced photochemical conditions, promoting condensation and particle growth (Venzac et al., 2008; Foucart et al., 2018). This study investigates PNSD measurements at CMN and JFJ to evaluate how ion concentrations and low condensation sink levels influence NPF in the FT. By focusing on these high-altitude sites, we aim to clarify the mechanisms driving NPF and their implications for aerosol abundance and cloud formation. The analysis is based

50 on approximately two years of observations at each station, describing seasonal variability and providing statistically robust comparisons.

2 Experimental

2.1 Measurement sites

Monte Cimone (CMN) and Jungfraujoch (JFJ) stations are among the few Global Atmosphere Watch (GAW)/World Meteo-
55 rological Organization (WMO) global stations located at high altitudes, where long-term ground-based monitoring of particle number size distributions has been performed for several years in fine and ultrafine size ranges. At both stations those measurement programs are conducted within the European ACTRIS research infrastructure (Laj et al., 2020).

Figure 1. Locations of the Monte Cimone (O. Vittori Observatory, CMN) and Jungfraujoch (Sphinx Laboratory, JFJ) stations. Map data © Esri, Maxar, Earthstar Geographics, GIS User Community, Stamen Design (CC BY 3.0), and OpenStreetMap contributors.

The Observatory "O. Vittori" on Monte Cimone (CMN, 44°12' N, 10°42' E) is located on the highest peak of the Northern Apennines, at 2165 m a.s.l.. Its strategic position, overlooking the Po Valley, allows air masses to reach the station from
60 any direction with a limited influence of orographic forcing (Cristofanelli et al., 2018; Vitali et al., 2024). This makes CMN an ideal site for studying aerosol dynamics driven by both regional and long-range transport. The observatory is considered representative of the Mediterranean and Southern European FT. However, it can be significantly affected by air masses from the PBL, particularly those originating in northern Italy and the highly polluted Po Valley, with this influence being most pronounced during summer daytime hours and diminishing at night, when the site predominantly reflects free tropospheric
65 characteristics (Cristofanelli et al., 2018; Rinaldi et al., 2015). The Sphinx Laboratory at the Jungfraujoch High Alpine Research Station (JFJ, 46.55° N, 7.98° E) is the highest observatory in Europe, located at an altitude of 3580 m a.s.l.. Situated on an exposed anticline in the Swiss Alps, between the Mönch and Jungfrau mountains, JFJ is an essential site for monitoring

atmospheric background conditions in Central Europe. The station predominantly experiences FT conditions during the winter
months (Herrmann et al., 2015), but also exhibits a significant influence of PBL, which makes it crucial to investigate the
70 transport of anthropogenic pollutants from the boundary layer. The site has been extensively characterized through almost 30
years of aerosol in situ measurements (Bukowiecki et al., 2016).

2.1.1 Instrumentation and data availability

Both research stations conduct particle number size distribution measurements following ACTRIS RI standards. At CMN, a
SMPS-TROPOS system is employed, combining a TROPOS Differential Mobility Analyzer (DMA) and a TSI 3750 Conden-
75 sation Particle Counter (CPC), operating continuously since 2017 with a 5-minute time resolution and a detection range of
10–800 nm. At JFJ, a custom-built SMPS system comprising a TSI 3071 DMA and a TSI 3775 CPC has been in operation
since 2018, with a time resolution of 10 minutes and a size detection range of 10–560 nm. Both systems are operated in
accordance with Wiedensohler et al. (2012), ensuring compliance with ACTRIS-RI quality assurance protocols. To measure
particles in the lower diameter range (<40 nm), both stations operate a Neutral Cluster and Air Ion Spectrometer (NAIS, Airel
80 Ltd., Estonia). The NAIS is designed to measure the mobility distributions of atmospheric positive and negative ions (0.8–40
nm), as well as total particles in the 2.5–40 nm range. It features two separate mobility analyzer columns, each dedicated to
one polarity. In ion mode, the aerosol sample is analyzed in its natural state, detecting only naturally charged particles. In total
particle mode, the sample passes through a preconditioning unit where particles are charged using ion currents generated by a
corona discharge. The lower detection limit for total particles (2.5 nm) is set by a post-filter, which regulates the concentration
85 of corona ions available for charging in the preconditioning stage (Manninen et al., 2009). The NAIS has been operational at
the JFJ site since 2019 through a collaboration with the Institute for Atmospheric and Earth System Research (INAR) at the
University of Helsinki. At CMN, the NAIS was installed in November 2021 and has been running continuously until now.
During the measurement period, the SMPS instruments at both CMN and JFJ were connected to a heated whole-air inlet de-
signed to sample aerosol particles and hydrometeors under laminar flow conditions (Re $\approx$ 2000). The inlet was maintained
90 at 25°C to promote the complete evaporation of cloud droplets and ice crystals. Consequently, under cloudy conditions, the
sampled aerosol included both interstitial and residual particles. The sample relative humidity (RH) was kept below 40%, in
accordance with GAW/WMO and ACTRIS recommendations. The NAIS inlet line at both stations consisted of a short (80
cm), electrically grounded, trace-heated copper tube, ensuring minimal diffusion losses and stable thermal conditions during
sampling. The data analysis presented in this paper refers to the simultaneous availability of NAIS and SMPS data for each
95 site. The CMN dataset comprises 646 measurement days from November 2021 to December 2023. At JFJ, data were collected
across 525 days between November 2019 and December 2022, albeit with more fragmented temporal coverage. Overall, the
datasets offer a well-distributed seasonal representation, with winter being the best-covered season at both sites (35.9% of total
data at JFJ and 31.2% at CMN). In contrast, summer months show notable data gaps (see Fig. S1).

3   Data Analysis

3.1   Instrument Harmonization and Data Processing

When operating in total particle mode, the NAIS may differ substantially from reference measurements, with reported discrepancies of up to an order of magnitude compared to SMPS data (Kangasluoma et al., 2020). Therefore, a detailed comparison was performed with the reference SMPS at both stations within overlapping size ranges: 20–30 nm for CMN and 30–40 nm for JFJ. Scaling factors were derived individually for each measured size distribution, and applied to all NAIS channels accordingly. The resulting mean scaling factors were 3.38±2.05 for CMN and 3.18±2.07 for JFJ. After scaling, NAIS and SMPS distributions were merged at 25nm for CMN and at 35nm for JFJ (see Fig. S2). The analyzed particle size distributions spanned a common range of 2.5–560nm for total particles and 0.8–40nm for ions. Particle number concentrations were categorized into four size modes reflecting dominant atmospheric processes. The intermediate mode (2.5–7nm) includes the smallest detectable particles, relevant to early-stage NPF. The nucleation mode (7–25nm) comprises freshly formed particles growing by condensation, whose survival depends on competition with coagulation. The Aitken mode (25–100nm) includes particles that may act as CCN upon sufficient growth. The accumulation mode (100–560nm) consists of aged particles shaped by long-range transport and chemical processing. Ions were likewise grouped into cluster ions (0.8–2nm), intermediate ions (2–7nm), and large ions (7–40nm). Number concentrations were calculated by integrating the particle number size distribution (dN/dlogDp) across each size class. Processed data were aggregated into 10-minute intervals for statistical analysis. Daily and monthly statistics (mean, standard deviation, median, and interquartile percentiles) were computed using only valid data. For further characterization, particle size distributions were fitted using a multi-lognormal distribution function with the updated DO-FIT algorithm (Hussein et al., 2005). Each mode i was defined by its number concentration (N_i), geometric mean diameter ($d_{pg,i}$), and geometric standard deviation (σ_i). The adaptive feature of the DO-FIT was enabled to determine the optimal number of modes needed to characterize each distribution without compromising fit quality beyond a defined tolerance.

3.2   New Particle Formation events Classification and Characterization

Atmospheric NPF events are characterized by rapid bursts of particles in intermediate and nucleation mode, originating from the nucleation of gas-phase precursors forming clusters approximately ($\sim$1–2nm) that subsequently grow into the Aitken mode. In this analysis, we applied a comprehensive approach by employing three classification methods to identify NPF events at the two stations. The first method, developed by Dal Maso et al. (2005), classifies NPF events through visual inspection and a decision tree. Events are classified into Class IA (clear and sustained NPF), Class IB (moderate events with less clarity or continuity), Class II (weak or incomplete NPF signatures), and Non-Events (no observable particle formation or growth). However, some days remain Undefined when they do not fit clearly into any category, creating inconsistencies in data analysis and interpretation. Furthermore, the method's reliance on subjective judgment introduces variability among observers, reducing classification reliability. Although originally designed for SMPS data, it has also been applied to merged NAIS–SMPS particle size distributions. The second approach, proposed by Dada et al. (2017), is a fully automated classification method that eliminates undefined days by assigning each day to one of four categories: Regional Events, Ion Bursts, Transported Events,

and Non-Events. It uses ion (2–4nm) and particle (7–25nm) concentrations, applying threshold criteria sustained over fixed durations (1h for ions, 1.5h for particles). This method requires NAIS data and is capable of distinguishing local versus transported NPF events. The third method, Nanoparticle Ranking Analysis (Aliaga et al., 2023), evaluates NPF intensity based on fluctuations in 3–6nm particle concentrations, a representative subset of the broader 2.5–7nm intermediate size range. The metric ΔN_{3-6} was smoothed using a two-hour rolling median. Rather than subtracting background concentrations as in the original study, we used a ratio-based intensity index:

$$NPF_{intensity} = \left(\frac{Max(\Delta N_{3-6})_{active}}{Median(\Delta N_{3-6})_{non-active}} \right) \tag{1}$$

This ratio, which compares peak daytime (09:00–16:00) to nighttime background (16:00–09:00) particle concentrations, serves as a continuous index of NPF intensity. For interpretative clarity, we discretised the continuous distribution using Gaussian fitting into four categories at each site: Intense, Moderate, Weak, and Negligible. Due to the persistent occurrence of a particle band in the 5–7nm range under high relative humidity (RH > 94%), likely related to cloud processing, automated classification methods by Aliaga et al. (2023) and Dada et al. (2017) were restricted to out-of-cloud periods. This band did not exhibit typical growth behavior and hindered NPF detection. Therefore, we limited inter-method comparisons to days with RH < 94%, when classifications were more reliable. NPF events were characterized by calculating the particle formation rate ($J_{2.5}$) and growth rate for particles in the 2.5–7nm range ($GR_{2.5-7}$). The formation rate was determined using the aerosol general dynamic equation (Kulmala et al., 2012), accounting for the time-dependent change in particle number concentration, coagulation losses, and particle growth:

$$J_{2.5} = \frac{dN_{[2.5-7)}}{dt} + \text{CoagS}_{2.5-7} \cdot N_{[2.5-7)} + \frac{GR_{2.5-7}}{(7-2.5)\,\text{nm}} \cdot N_{[2.5-7)} \tag{2}$$

where $N_{[2.5-7)}$ is the particle concentration and $CoagS_{2.5-7}$ is the coagulation sink, which quantifies particle loss due to coagulation. The $GR_{2.5-7}$ was obtained using the maximum concentration method, applying a rolling median and Gaussian filter to identify peak concentration times and performing a linear fit (Kulmala et al., 2012). Additionally, the condensation sink (CS) describes the scavenging of condensing vapors by pre-existing aerosols. It was calculated based on the aerosol number size distribution and sulfuric acid diffusivity. Further details regarding these calculations are provided in Supplementary Material Section S3.

3.3 In-cloud and out-of-cloud conditions

To investigate the influence of atmospheric conditions on PNSD and NPF, we classified measurement periods as either in-cloud or out-of-cloud. Since routine liquid water content (LWC) measurements were unavailable at both stations, we used relative humidity (RH) as a proxy to distinguish between these conditions. Threshold RH values were determined through density plot analysis and by assessing the effect of RH on particle size distributions in the size range below SMPS detection limit, using only NAIS measurements. Our analysis revealed that when RH was below 94%, particle size distributions remained stable, allowing us to confidently classify these days as out-of-cloud. In contrast, in-cloud conditions were defined as days when RH exceeded 97%, consistent with (Herrmann et al., 2015). Webcam images were used to further validate cloud presence at the stations.

4 Results

4.1 Overview of particle distribution at JFJ and CMN

4.1.1 Number Concentration Properties

Median aerosol particle concentrations in the 2.5–560nm size range were higher at CMN ($1219 cm^{-3}$) than at JFJ (770^{-3}), consistent with the expected range for high-altitude stations (Laj et al., 2020). CMN also exhibited a wider interquartile range (1296^{-3} vs. 962^{-3} at JFJ), indicating greater variability in particle abundance, likely driven by stronger boundary layer influence. When examining the particle number size distribution across four defined mode, i.e. intermediate (2.5–7nm), nucleation (7–25nm), Aitken (25–100nm), and accumulation (100–560nm), distinct site-specific patterns emerge (Table 1).

	CMN					JFJ				
	$N_{2.5-7}$	N_{7-25}	N_{25-100}	$N_{100-560}$	N_{tot}	$N_{2.5-7}$	N_{7-25}	N_{25-100}	$N_{100-560}$	N_{tot}
Mean	273.5	546.0	665.0	302.2	1786.6	379.5	442.1	336.1	165.9	1323.6
Median	65.0	220.2	443.2	176.2	1218.9	91.5	197.3	222.4	68.6	770.2
SD	909.4	1179.8	777.4	322.7	2252.3	1654.2	993.3	384.7	234.6	2387.3
25th percentile	27.6	100.5	253.1	60.3	733.5	41.2	96.4	126.6	32.8	482.7
75th percentile	182.6	525.8	776.5	449.2	2029.0	231.9	424.7	404.1	177.7	1444.6

Table 1. Descriptive statistics of particle number concentrations at CMN and JFJ across different size modes. The unit of measurement for each N is $[cm^{-3}]$.

JFJ exhibits a higher relative contribution of smaller particles, with the intermediate mode contributing 26.5% of total particles compared to 14.1% at CMN, and nucleation mode making up 32.2% at JFJ versus 28.8% at CMN. While this suggests a higher fraction of small clusters at JFJ, it does not necessarily indicate more efficient particle formation, as these clusters must survive and grow into larger sizes to contribute to total aerosol load. Aitken-mode particles dominate the number concentration at CMN, accounting for 38.9% of total particles versus 27.1% at JFJ, suggesting that more freshly nucleated particles at CMN successfully grow beyond the smallest size ranges. It also reflects greater exposure to regional transport and anthropogenic influences at CMN, particularly from the Po Valley. Accumulation-mode particles accounted for 18.2% of the total at CMN and 14.2% at JFJ, indicating comparable but slightly higher aged aerosol load at CMN (see Fig. 2 for modal contributions).
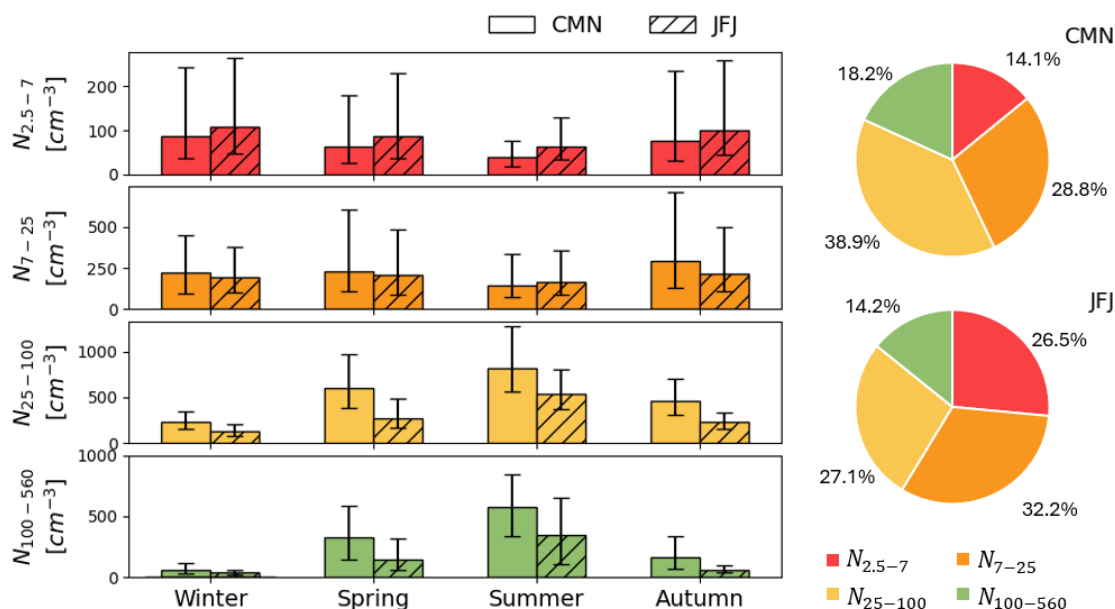
Figure 2. On the left, seasonal median particle number concentrations are presented for CMN (empty box) and JFJ (crossed-line box) across different size ranges, with whiskers indicating the interquartile ranges. On the right, the percentage contribution of each particle size mode to the total number concentration is shown, with CMN shown at the top and JFJ at the bottom.

Fig. 3 shows the seasonal variability in total concentrations, which peak in summer (CMN: $1743 cm^{-3}$, JFJ: $1360 cm^{-3}$) and reach their lowest in winter (CMN: $718 cm^{-3}$, JFJ: $568 cm^{-3}$). This seasonal pattern is mainly driven by the Aitken and accumulation modes, which increase substantially in warm months due to enhanced boundary layer activity (Rose et al., 2021; Herrmann et al., 2015). Aitken-mode concentrations at CMN were four times higher in summer ($814 cm^{-3}$) than in winter
185 ($229 cm^{-3}$), while accumulation-mode concentrations increased ninefold (580 vs. $57 cm^{-3}$). A similar pattern is observed at JFJ, although with lower summer-to-winter ratios: Aitken-mode concentrations are approximately four times higher in summer, while accumulation-mode concentrations increase by a factor of eight. Unlike larger particles, intermediate and nucleation mode concentrations exhibit a different seasonal pattern. The intermediate mode is consistently more abundant at JFJ, with a winter maximum and summer minimum at both sites. Nucleation-mode concentrations were slightly higher at CMN, particu-
190 larly in spring and autumn, indicating more efficient growth of newly formed particles. Unlike larger particles, intermediate- and nucleation-mode concentrations do not follow the strong summer peak seen in Aitken and accumulation modes.
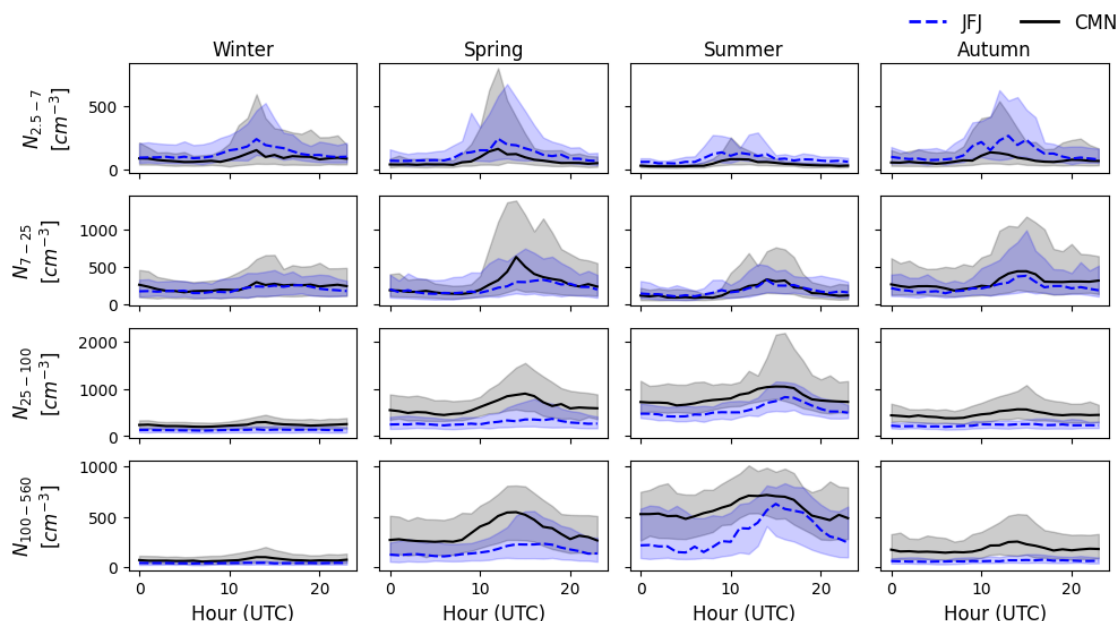
Figure 3. Diurnal variation of particle number concentrations across four modes (intermediate 2.5–7 nm, nucleation 7–25 nm, Aitken 25–100 nm, and accumulation 100–560 nm) for each season is shown for the CMN (solid line) and JFJ (dashed line) stations. All times are in UTC.

Diurnal patterns at CMN and JFJ (Fig. 3) show that intermediate particles remain relatively stable throughout the day, with a slight midday increase aligning with peak solar radiation. However, larger variations in the interquartile range (IQR) indicate that nucleation events are episodic, with pronounced midday peaks (10:00–12:00 UTC) in all seasons at both sites. These peaks

195 are particularly evident in spring and autumn, suggesting a seasonally varying nucleation activity. The nucleation mode shows a clear progression of particle growth beyond the smallest clusters, peaking shortly after the intermediate mode, showing that a fraction of freshly formed particles successfully grow past the critical survival size. This growth is most evident in spring and autumn, while in summer, a limitation in nucleation efficiency reduces the intensity of this cycle. In contrast, Aitken and accumulation mode particles peak later in the afternoon, reflecting both the growth of nucleated particles and contributions

200 from boundary layer transport. Their stronger diurnal cycle in summer indicates an increased influence of vertical transport, whereas the flatter winter trend suggests a reduced role of boundary layer dynamics. A notable contrast is observed in autumn, where JFJ shows a flatter diurnal pattern, whereas CMN maintains more pronounced daily fluctuations, likely due to stronger local-scale influences on particle growth and transport.

4.1.2   Modal Structure of the Particle Size Distribution

205 The particle number size distribution at CMN and JFJ was initially divided into four a priori modes (intermediate, nucleation, Aitken, accumulation), based on commonly used size ranges in aerosol studies, as described in the Data analysis section. These categories reflect distinct stages of aerosol evolution from freshly nucleated particles to aged, optically and climatically active

particles. These modes reflect distinct stages of particle growth and transformation. However, detailed analysis of hourly size distributions using multi-lognormal fitting revealed that five statistically distinct modes more accurately capture the variability

210 and structure at both stations. These modal characteristics are summarized in Table 2.

	CMN			JFJ		
	d_{pg} [nm]	σ	N[cm^{-3}]	d_{pg} [nm]	σ	N[cm^{-3}]
Mode 1	2.6	1.6 (1.4-1.9)	297 (78-900)	2.4	1.6 (1.4-2.0)	226 (101-544)
Mode 2	9.6	1.7 (1.5-2.0)	398 (193-748)	9.8	1.7 (1.5-2.0)	293 (148-574)
Mode 3	37.4	1.5 (1.4-1.7)	225 (90-534)	32.2	1.6 (1.5-1.7)	184 (99-368)
Mode 4	137.8	1.5 (1.4-1.6)	27 (2-124)	91.4	1.5 (1.4-1.7)	48 (11-116)
Mode 5	507.2	1.5 (1.4-1.7)	2 (1-15)	332.7	1.6 (1.4-2.0)	8 (4-26)

Table 2. Statistics of modal structure for hourly particle number size distributions. The table presents the median and 25th-75th percentiles for each of the five modes at each station, including the mean geometric diameter (d_{pg}), standard deviation (σ), and particle number concentration (N) for each log-normal mode.

The frequency spectrum of fitted modes based on their d_{pg} and N is illustrated in Fig. 4. At CMN (left panel), the distribution spans a wide range of sizes and concentrations, with five modal clusters clearly distinguishable. These correspond to the cluster/intermediate mode ($\sim$2–3nm), early nucleation ($\sim$10nm), late nucleation–Aitken ($\sim$30–40nm), small accumulation ($\sim$140nm), and large accumulation ($\sim$500nm). The high variability in both modal size and concentration reflects frequent

215 NPF activity and dynamic boundary layer interactions. In contrast, the modal structure at JFJ (right panel) is more compact, with two dominant lobes consistently centered around $\sim$30nm and $\sim$90nm. These persistent modes suggest a more stable and homogeneous aerosol population, influenced by less variable conditions in the free troposphere. It is important to note that the absolute frequency of fitted modes is affected by the length of data coverage, which is longer at CMN. Therefore, comparisons should focus on structural patterns, such as mode position and spread, rather than frequency magnitude.
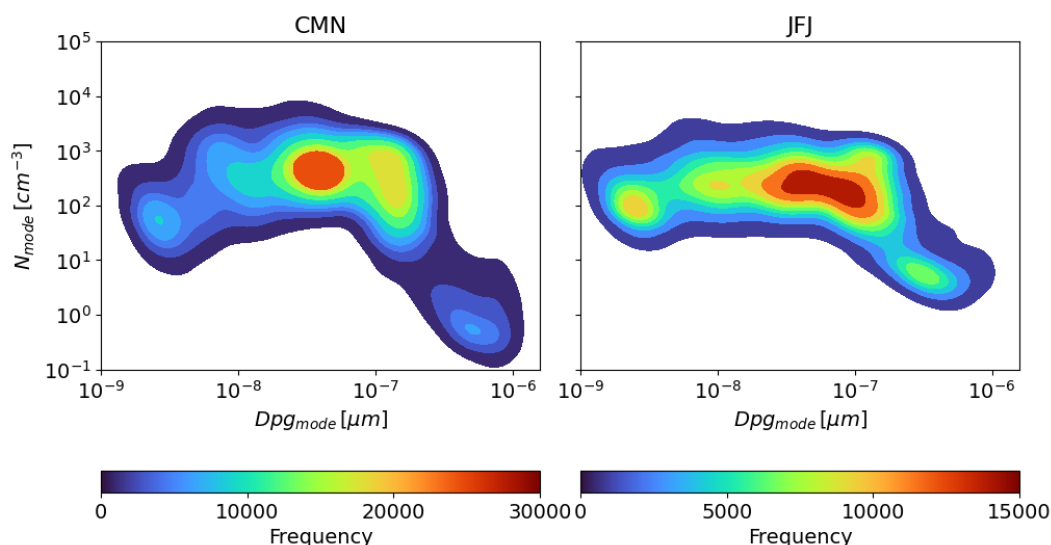
Figure 4. Modal structure spectrum of the particle number size distribution derived from the multi-lognormal distribution fitting (hourly average) at CMN (left) and JFJ (right).

4.1.3 Ion properties

Ions may play a critical role in atmospheric NPF, particularly in environments where ion-induced nucleation enhances the stability of newly formed clusters. Fig. 5 presents the median concentrations (with interquartile ranges) of positive and negative ions at CMN and JFJ, separated into cluster (0.8–2 nm), intermediate (2–7 nm) and large (7–40 nm) size classes; the lower panels report the positive-to-negative ratios. At both sites, positive cluster ions were significantly more abundant than their negative counterparts. The median concentrations at CMN were $373\,cm^{-3}$ and $63\,cm^{-3}$ for positive and negative cluster ions, respectively, yielding a positive-to-negative ratio of 5.5. JFJ exhibited a similar but slightly more pronounced polarity imbalance, with a ratio of 7.3 ($309\,cm^{-3}$ vs. $35\,cm^{-3}$). These elevated ratios has been observed at other ground stations, such as Chacaltaya (Bolivia), Izaña (Spain) and Zeppelin (Norway) (Aliaga D., Agrò M., Heslin-Rees D., personal communication) and suggest a preferential formation or longer atmospheric lifetime of positively charged clusters. While laboratory calibrations do not reveal systematic biases between polarities, environmental factors and ion chemistry likely contribute to the observed asymmetry. Variations in core ion composition, precursor availability, and ion sink mechanisms could influence ion mobility and size distributions, particularly in the cluster and intermediate size ranges. Additionally, topographic effects and the associated atmospheric electric fields at mountain sites may play a role in modulating ion charge distributions. One more possible explanation for the relative abundance of positive cluster ions compared to negative ones is measurement limitations at lower atmospheric pressures, such as those found at mountain sites. Due to their higher mobility, negative ions may move beyond the detectable size range, leading to an underestimation of their concentrations (Hirsikko et al., 2011). Further investigation is warranted to disentangle instrumental, chemical, and physical drivers of these charge distributions.

In the intermediate size range, the charge asymmetry decreased substantially. At CMN, positive and negative ion concentrations were nearly balanced, with a median ratio of 1.2, while JFJ showed a slight dominance of negative ions, yielding a median ratio of 0.8. For large ions (>7 nm), the positive-to-negative ratios at both sites converged toward unity (1.0 at CMN and 0.9 at JFJ), suggesting that once particles reach larger sizes, charge distribution equilibrates.
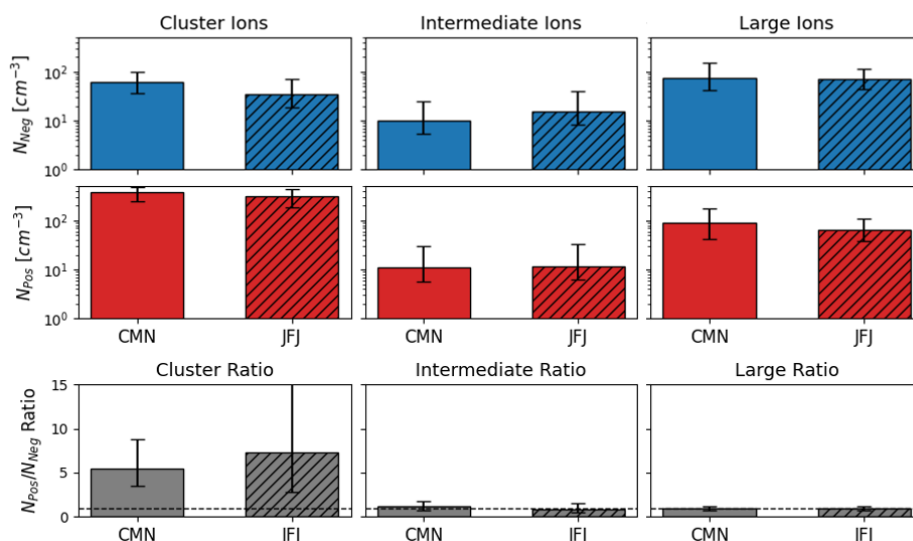
Figure 5. Median concentrations and interquartile ranges of negative (blue) and positive (red) ions at CMN and JFJ, grouped into three size categories: cluster (<2 nm), intermediate (2.5–7 nm), and large (>7 nm). Hatching indicates JFJ. The bottom row shows the median positive-to-negative ion concentration ratios for each size range.

4.2 In-Cloud and Out-of-Cloud conditions

The presence of clouds significantly affects PNSD at both sites. Figure 6 presents the median PNSDs at the CMN and JFJ sites under contrasting relative humidity conditions, used here as a proxy for cloud presence. Periods with RH<94% (orange lines) are considered out-of-cloud, while RH>97% (blue lines) is interpreted as in-cloud, supported by time-synchronized webcam imagery confirming immersion of the stations within cloud layers.
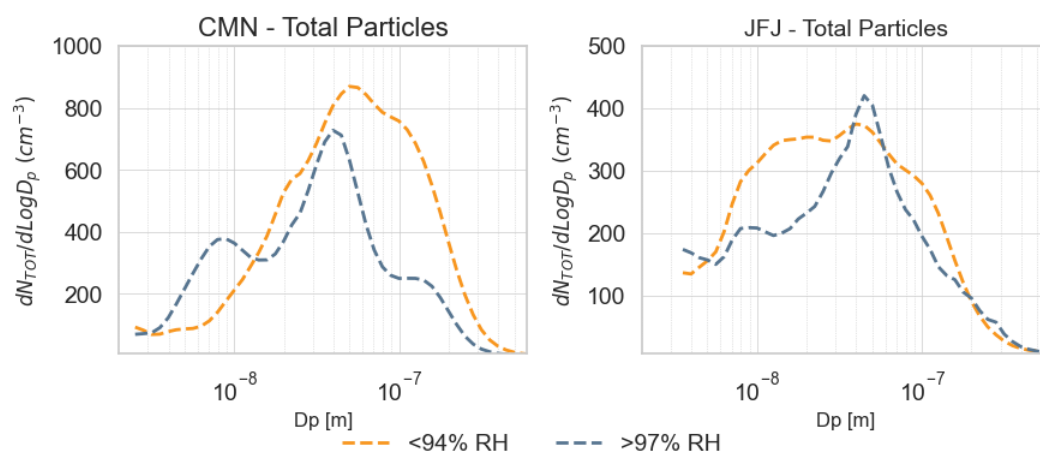
Figure 6. Median particle number size distributions (PNSD) for particles at the CMN (left) and JFJ (right) measurement stations under varying relative humidity (RH) conditions. The orange dashed lines indicate out-of-cloud conditions (RH < 94%), while the blue dashed lines represent in-cloud conditions (RH > 97%).

At CMN, in-cloud conditions are associated with a substantial modification of the PNSD. Compared to out-of-cloud periods, a pronounced depletion is observed in the accumulation mode (>50 nm), with number concentrations reduced by up to a factor of three near the 80 nm peak. This reduction is consistent with efficient cloud scavenging of CCN-sized particles. Concurrently, a distinct mode appears below 10 nm, centred around 8 nm, which is absent or weak during out-of-cloud conditions. This newly emergent nucleation mode substantially increases the number concentration of ultrafine particles in the sub-10 nm range, resulting in a bimodal structure under in-cloud conditions. The appearance of this mode may indicate cloud-related new particle formation or potential instrumental artefacts under high humidity conditions, such as fragmentation of larger charged particles in the corona-based charger. However, the systematic nature and timing of the signal suggest a physical origin cannot be excluded.

At JFJ, similar but less pronounced trends are observed. In-cloud conditions lead to a downward shift in accumulation-mode particle concentrations, although the effect is less dramatic than at CMN. Interestingly, the in-cloud PNSD exhibits a peak around 50–60nm, slightly larger than the typical Aitken mode peak seen during out-of-cloud periods. This may reflect the partial activation of smaller particles near the CCN activation threshold, allowing particles below 50 nm to remain in the interstitial phase. As at CMN, a modest enhancement in sub-10nm particle concentrations is observed during in-cloud conditions, with a peak around ∼9nm.

These observations suggest a consistent response of aerosol size distributions to cloud processing at both sites, marked by scavenging of larger particles and possible in-cloud production or transformation of ultrafine particles. The stronger signal at CMN may reflect site-specific differences in cloud microphysics, air mass origin, or instrument sensitivity.

Ions also shows different behaviour between out-of- and in-cloud at both sites (Fig. 7). Concerning negative ions, the size distribution at CMN shows minimal variation when cloud forms, while the positive ions show a strong reduction in the cluster-ion

range, with median values decreasing from $364cm^{-3}$ (IQR: 241-477cm^{-3}) to $66cm^{-3}$ (IQR:41-204cm^{-3}). Similar behaviour is observed at JFJ, where the median drops from 317 cm^{-3} (IQR:196-430cm^{-3}) to $148cm^{-3}$ (IQR:61-323cm^{-3}). Similar evidence was observed at Puy de Dôme, where cloud scavenging has been identified as a dominant sink for cluster ions, with the process being particularly efficient for positive ions (Venzac et al., 2007). At CMN, intermediate ions remain nearly unchanged between in-cloud and out-of-cloud conditions, similar to observations at Puy de Dôme, while at JFJ, a slight increase in ion concentrations is observed for both positive (growing from $10cm^{-3}$ (IQR:6-25cm^{-3}) to $14cm^{-3}$ (IQR:7-49cm^{-3})) and negative intermediate ions, (increasing from $14cm^{-3}$ (IQR:8-30cm^{-3}) to $24cm^{-3}$ (IQR:12-95cm^{-3})). Large ions do not exhibit significant differences between in-cloud and out-of-cloud conditions, except for a slight increase observed in-cloud for both positive and negative large ions at JFJ. Specifically, negative large ions increase from a median of $68cm^{-3}$ (IQR: 46-106cm^{-3}) to $96cm^{-3}$ (IQR: 69-135cm^{-3}), and positive large ions rise from $61cm^{-3}$ (IQR: 40-100 cm^{-3}) to $86cm^{-3}$ (IQR: 62-118 cm^{-3}).
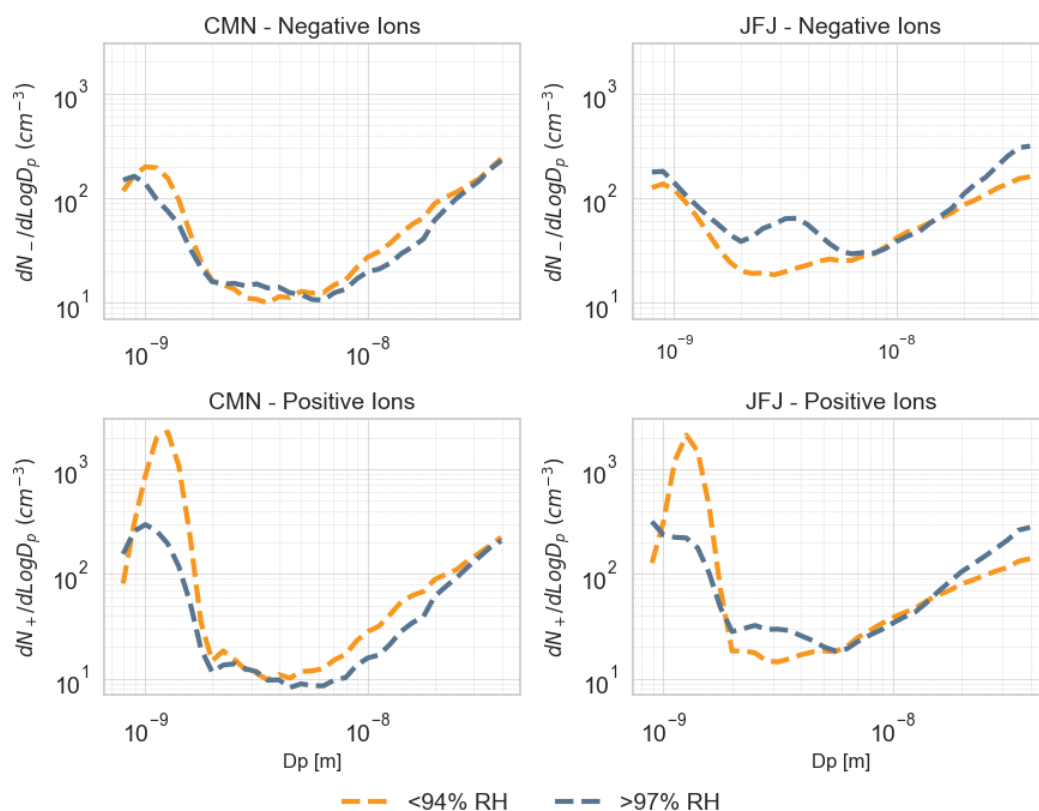
Figure 7. Median particle size distributions (PSD) for negative ions (left column), positive ions (middle column), and total particles (right column) at the CMN (top row) and JFJ (bottom row) measurement stations under varying relative humidity (RH) conditions. The blue dashed lines indicate out-of-cloud conditions (RH < 94%), while the orange dashed lines represent in-cloud conditions (RH > 97%).

4.3 Seasonal NPF event frequency across classification methods

NPF event frequencies at CMN and JFJ were evaluated under out-of-cloud conditions using three established classification
280 methods: the visual decision tree of Dal Maso et al. (2005), the ion-based threshold method of Dada et al. (2017), and the
intensity-based ranking by Aliaga et al. (2023). This multi-method approach enables cross-validation of results and deeper
insight into the seasonal and site-specific characteristics of NPF at these two high-altitude GAW stations. The final dataset
comprises 438 days at CMN and 391 days at JFJ. As shown in Fig. 8, all three methods indicate consistently higher NPF
activity at CMN compared to JFJ. According to the Dal Maso classification, events (Class IA, IB, and II combined) occurred
285 on 32% of valid days at CMN and 13% at JFJ. CMN exhibited pronounced spring peaks in strong events (e.g., 21.6% Class IA
days in April), while JFJ showed weaker signals and a higher proportion of Undefined days (36.6%), often associated with
nucleation-mode particles that do not clearly grow into the Aitken range. The Dada method corroborates these findings, with
CMN dominated by Regional and Transported events, particularly in spring and autumn, while JFJ exhibited fewer Regional
events and a greater share of Burst-type NPF episodes. Burst events, especially in February and summer at JFJ, suggest transient
290 nucleation events limited by unfavorable growth conditions. The nanoparticle ranking analysis further confirms the higher NPF
intensity at CMN, where Intense and Moderate events together account for 28% of days, with maximum frequencies in March
and November. In contrast, JFJ records 17% of days as Intense or Moderate, with most days (51%) classified as Negligible.
Monthly trends shown in Fig. 8 reveal a strong springtime seasonality in all schemes, but with consistently more frequent
and more intense events at CMN. This difference is likely driven by CMN's lower elevation, stronger coupling with boundary
295 layer dynamics, and proximity to the Po Valley, which provide higher precursor availability. JFJ, located deeper in the free
troposphere, appears more frequently influenced by transported air masses and exhibits a more stable background of small
ions and particles that rarely transition into fully developed NPF events. Despite differences in classification criteria, all three
methods converge on a coherent picture: NPF events are more frequent, more intense, and more variable at CMN, while JFJ is
characterized by fewer events and a higher occurrence of weak or indeterminate cases, reflecting their contrasting atmospheric
300 environments. Complete event statistics and cross-method correspondences are reported in Tables S1–S3 in the Supplementary
Material.
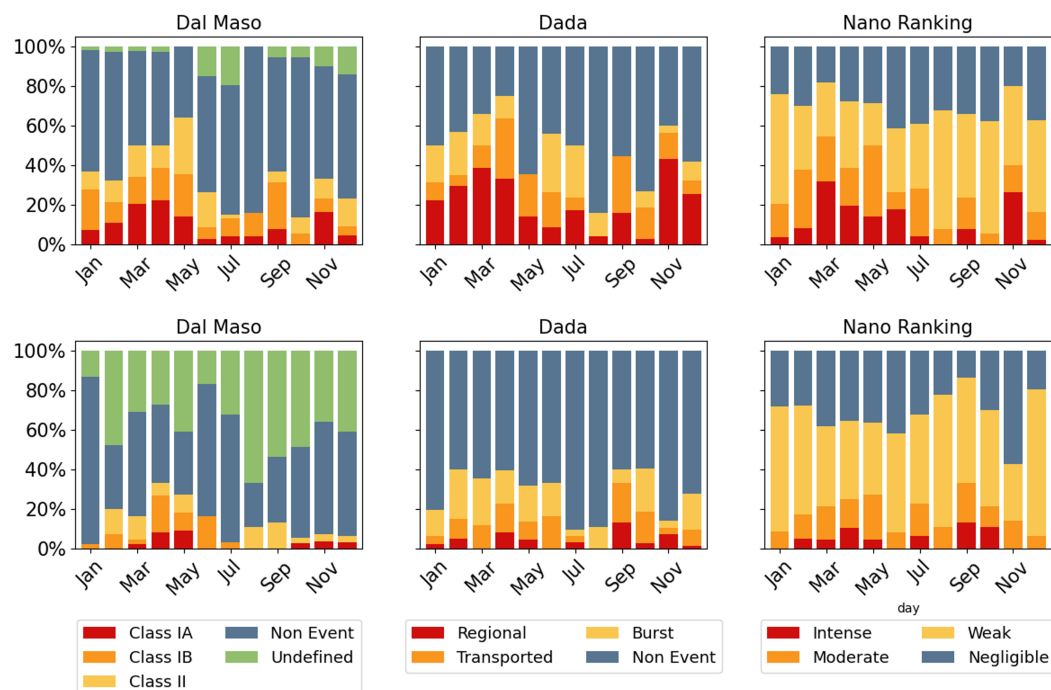
Figure 8. Comparison of classification methods for NPF events. The Dal Maso method (right), Dada method (center), and nanoparticle ranking method (left) are compared, showing the monthly frequency of events typical at CMN (top) and JFJ (bottom).

4.4 Diurnal variation of neutral and charged particles during NPF

On days with intense NPF events, the intermediate (2.5–7 nm) particle concentration shows a clear diurnal variation at both sites, in contrast to negligible event days. As shown in Fig. 9 at CMN the number concentration increases in a well-defined pattern, peaking around 11:00 at approximately $2260 cm^{-3}$, while at JFJ the peak is broader with a first one observed at 9:00 and the second main peak at 13:00. The nucleation mode diel at CMN follows the intermediate peak, reaching its maximum around 13:00 with approximately $1525 cm^{-3}$. At JFJ, although the peak is less pronounced it reaches a maximum around 15:00. The Aitken mode shows a similar behaviour as the nucleation particles, with higher concentrations. Concerning the accumulation mode, CMN doesn't show significant differences between intense and negligible NPF events, while at JFJ, an increase of accumulation particles is observed in the afternoon during intense NPF events, indicating a possible influence of vertical transport (peaking in the afternoon) on NPF occurrence, such as NPF triggered at interface between clean conditions and PBL injection.
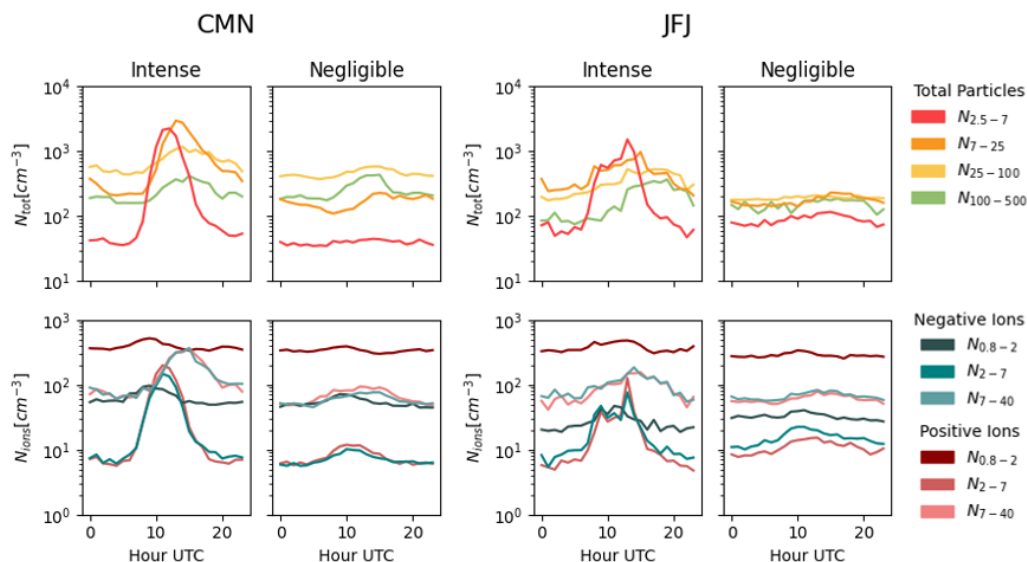
Figure 9. Diurnal variations of total particle number concentrations N_{tot}, negative ion concentrations and positive ion concentrations N_{ions}, at two sites CMN (left panel) and JFJ (right panel). Data is shown for Intense and Negligible NPF days. The legend provides particle size ranges with corresponding color codes for total particles, negative ions, and positive ions. Units for all concentrations are in $[cm^{-3}]$, and time is shown in UTC hours.

Regarding the ions, the concentration of positive cluster ions remains consistently higher throughout the day at both stations. Although the diurnal variation is generally flat, it becomes more evident on days with Intense NPF events, indicating a clear

315   link between particle formation intensity and ion concentration. A similar behaviour is observed for negative cluster ions, but here the diurnal variation is even more pronounced, particularly at JFJ, suggesting that negative ions may be more sensitive to the nucleation process. Negative cluster ions, indeed, show deeper diurnal variation during NPF events due to their strong affinity for acidic precursors like sulfuric acid, which stabilize early clusters. Rose et al. (2018) highlighted their critical role in nucleation, particularly at high-altitude sites where ion pair production is enhanced. Intermediate ions show a daily

320   variation that mirrors the pattern seen for intermediate particles, regardless of polarity, and this behaviour is consistent at both measurement sites. For large ions, the daily variation is aligned with that of Aitken particles, with concentrations rising during intense NPF events, reflecting the increased particle production. On days with negligible NPF activity, the ion concentration patterns remain almost flat. This suggests that ion concentrations are tightly coupled to the NPF occurrence. These observations align with findings from the CLOUD experiment by Wagner et al. (2017), which demonstrated that ions enhance the nucleation

325   process by stabilizing newly formed clusters, particularly under conditions where neutral clusters are unstable. The study also observed that a significant fraction of clusters carried a charge at 1.5 nm diameter, highlighting the role of ions in the early stages of particle formation.

4.5 Variables Affecting NPF

To investigate the atmospheric conditions that control NPF, we analyzed the meteorological variables and condensation sink
330 (CS) under out-of-cloud conditions, grouping days by NPF intensity (intense vs. negligible) as determined by the nanoparticle
ranking method. At both stations, intense NPF events are associated with higher solar radiation and lower RH, indicating
that photochemical activity is a key driver and that elevated RH may suppress nucleation, potentially by reducing precursor
vapor availability. Temperature and wind speed showed site-dependent behavior: at CMN, warmer temperatures coincided
with intense NPF, while at JFJ, temperature differences between intense and negligible events were less distinct, suggesting a
335 weaker influence. Wind speed exhibited site-specific patterns. At CMN, winds were slightly stronger during the early hours
preceding intense nucleation events compared to negligible days, potentially supporting precursor transport. In contrast, wind
at JFJ remained relatively constant throughout the day, with higher speeds generally associated with a suppression of NPF,
likely due to enhanced dilution and reduced precursor residence time.

To further understand particle survival conditions, we examined the CS between 06:00 and 09:00 UTC, the hours preceding
340 typical nucleation onset. As shown in Fig. 10, CS was consistently lower on intense NPF days compared to negligible ones,
except in autumn at JFJ where values were similar. At CMN, this difference was especially pronounced in summer ($3.2 \times
10^{-3} s^{-1}$ vs. $8.6 \times 10^{-3} s^{-1}$), while at JFJ, a smaller contrast was observed ($0.9 \times 10^{-3} s^{-1}$ vs. $4.4 \times 10^{-3} s^{-1}$). This seasonal
variability aligns with the role of precursor and condensable vapours availability in high-altitude environments, where lower CS
favours nucleation by reducing competition for condensable species (Sellegri et al., 2019), whereas higher CS can inhibit new
345 particle formation, favouring the growth of existing particles. These findings highlight the importance of clean atmospheric
conditions in enabling nucleation and early particle growth.
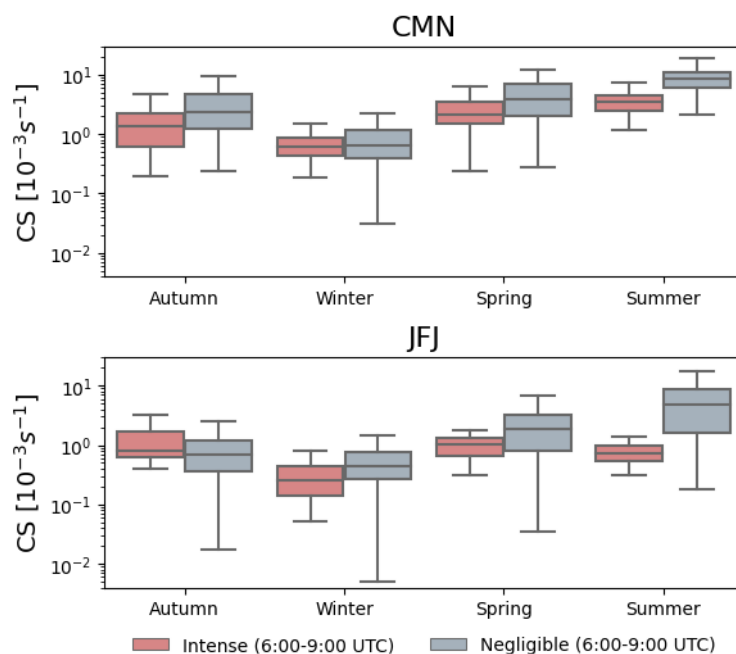
Figure 10. Seasonal variation in Condensation Sinks (CS) at CMN (top panel) and JFJ (bottom panel) stations. Boxplots represent the logarithmic distribution of CS [$10^{-3}s^{-1}$] during intense and negligible event periods (6:00–9:00) for each season.

4.6 Particle Formation and Growth Rates

To assess the particle formation and growth dynamics during NPF events, we analyzed the formation rate $J_{2.5}$ and growth rate $GR_{2.5-7}$ under intense event conditions. Table 3 presents their seasonal averages and standard deviations at CMN and JFJ.

350   At both stations, $J_{2.5}$ exhibited a clear seasonal cycle, with the highest values in spring and the lowest in summer. CMN recorded peak formation rates in spring ($1.27 \pm 1.73\,\text{cm}^{-3}\,\text{s}^{-1}$) and minimum rates in summer ($0.36 \pm 0.22\,\text{cm}^{-3}\,\text{s}^{-1}$), while JFJ followed a similar pattern but with overall lower values, ranging from $0.90 \pm 0.77\,\text{cm}^{-3}\,\text{s}^{-1}$ in spring to $0.20\,\text{cm}^{-3}\,\text{s}^{-1}$ in summer. These results highlight the importance of photochemical activity and precursor availability in driving nucleation, particularly during spring.

355   Growth rates $GR_{2.5-7}$ revealed distinct site-specific patterns. CMN exhibited the highest values in summer and spring (5.76 and $5.26\,\text{nm h}^{-1}$, respectively), indicating favorable conditions for sustained particle growth, possibly due to enhanced biogenic vapors and low condensation sinks. At JFJ, growth rates peaked in spring ($4.15\,\text{nm h}^{-1}$) and autumn ($3.12\,\text{nm h}^{-1}$), but remained significantly lower in summer and winter. This may reflect reduced vapor availability or stronger dilution effects in the free troposphere.

360   These seasonal dynamics are consistent with previous high-altitude studies. Boulon et al. (2011) reported average $J_2 \approx 1.4\,\text{cm}^{-3}\,\text{s}^{-1}$ and growth rates above 6 nm h^{-1} at Puy de Dôme, while Tröstl et al. (2016) observed $J_{3.2} \approx 1.8\,\text{cm}^{-3}\,\text{s}^{-1}$ at JFJ.

More broadly, Nieminen et al. (2018) identified spring as the typical peak for mountain NPF, driven by enhanced radiation and precursor gas production.

Figure 11 illustrates the relationship between $J_{2.5}$, $GR_{2.5-7}$, and the NPF intensity factor. Each percentile bin of intensity
365 is color-coded by the average background concentration of 3–6 nm particles (N_{3-6}). At CMN, both metrics increase with intensity, especially for growth rates, which rise from below 0.5 to over 3 nm h^{-1} across the intensity spectrum. At JFJ, the increase in $GR_{2.5-7}$ with NPF intensity is weaker and more scattered, with less evident separation between intensity bins. Despite JFJ exhibiting a consistently higher background of small particles, this does not translate into faster growth, suggesting that the conditions at CMN are more favorable for sustaining particle growth during strong nucleation events.

370 A similar pattern holds for $J_{2.5}$: while values are comparable between sites at low and intermediate intensities, CMN displays a sharper increase above the 90th percentile, reaching up to 1.0 cm^{-3} s^{-1} compared to 0.6 cm^{-3} s^{-1} at JFJ. This shift suggests that, although JFJ maintains a persistent presence of intermediate-sized particles, CMN is more capable of sustaining strong nucleation events under the right atmospheric conditions.

	$J_{2.5}$ $[cm^{-3}s^{-1}]$		$GR_{2.5-7}$ $[nm\,h^{-1}]$	
	CMN	JFJ	CMN	JFJ
Spring	1.27 ± 1.73	0.90 ± 0.77	5.26 ± 3.07	4.15 ± 3.74
Summer	0.36 ± 0.22	0.20	5.76 ± 5.64	1.39
Autumn	0.71 ± 0.54	0.34 ± 0.25	2.48 ± 0.89	3.12 ± 0.52
Winter	1.02 ± 0.77	0.21 ± 0.51	4.85 ± 4.33	2.37 ± 2.41

Table 3. Seasonal variability of particle formation rates $J_{2.5}$ and growth rates $GR_{2.5-7}$ at CMN and JFJ. Values are presented as mean $\pm$ standard deviation.

(a)

(b)
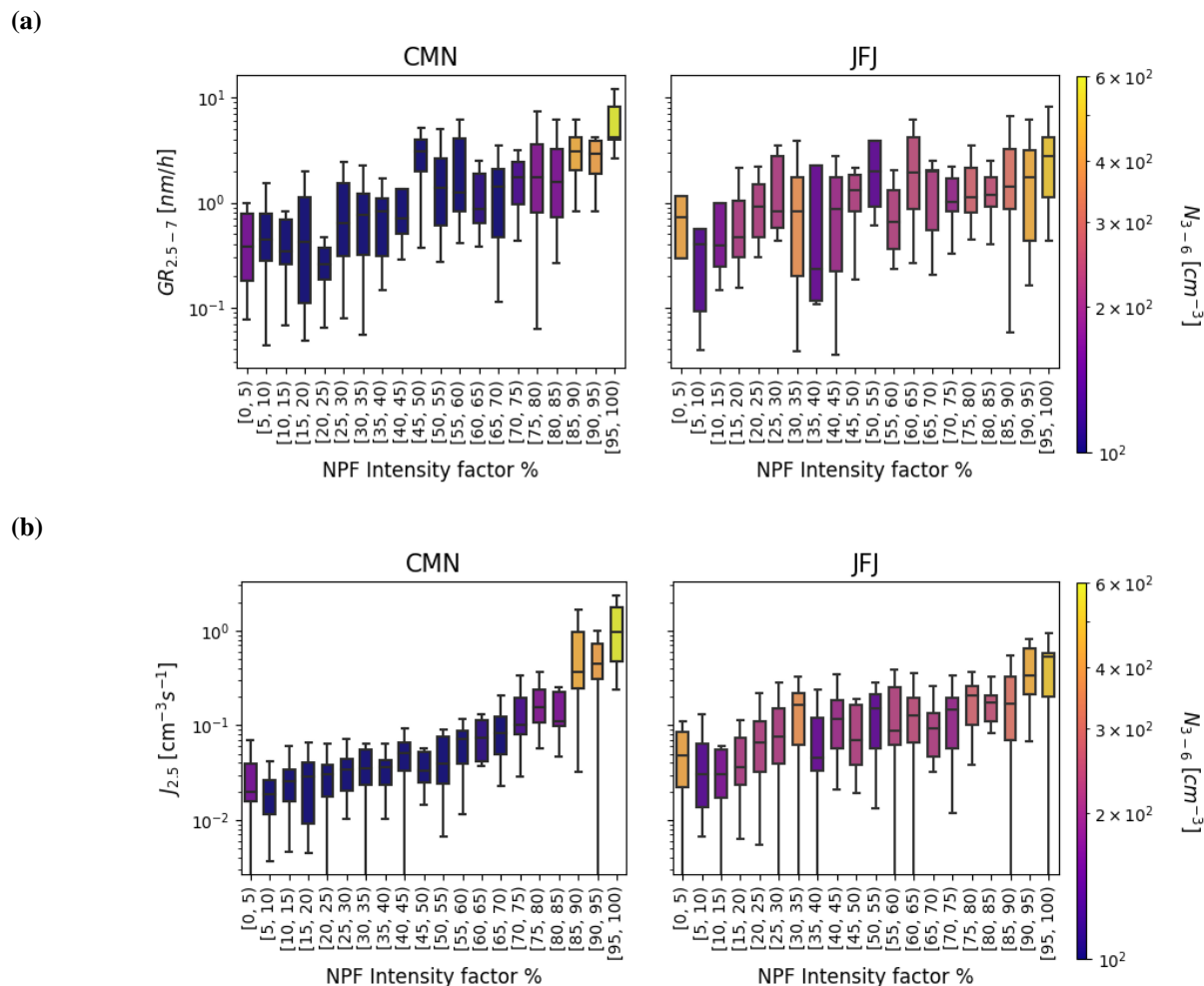
Figure 11. (a) Particle growth rate $GR_{2.5-7}$ and (b) formation rate $J_{2.5}$ as a function of NPF intensity at CMN and JFJ. Each percentile bin is color-coded by the average background particle concentration (N_{3-6}).

5 Conclusions

375 This study presents a comprehensive comparison of aerosol number size distributions and new particle formation (NPF) processes at two high-altitude GAW stations, Monte Cimone (CMN, 2165 m a.s.l.) and Jungfraujoch (JFJ, 3580 m a.s.l.), based on approximately two years of harmonized SMPS and NAIS measurements. By employing three established classification methodologies, we provide a robust assessment of NPF event frequency and intensity, alongside particle formation and growth characteristics, in the European free troposphere (FT).

380 Both stations exhibited a clear seasonal cycle in aerosol number concentrations, with maxima during summer driven primarily by boundary layer (PBL) influence and minima in winter reflecting cleaner FT conditions. Annual median particle concentrations (2.5–560 nm) were consistently higher at CMN, reflecting a stronger influence from the underlying boundary

layer and regional pollution sources such as the Po Valley. In contrast, JFJ exhibited a relatively larger contribution of sub-25 nm particles, in the intermediate and nucleation modes. However, particle growth into the Aitken mode was more efficient at CMN, suggesting that FT–PBL interface favors both nucleation and sustained particle growth due to enhanced precursor availability and photochemical activity.

NPF events occurred more frequently and were more intense at CMN than at JFJ across all classification methods, with maximum frequencies in spring and autumn. Diurnal profiles confirm that NPF at both sites typically initiates mid-morning and peaks in the early afternoon, aligned with solar radiation and photochemical conditions. At JFJ, the higher frequency of weak or indeterminate events suggests a persistent background of small charged particles without consistent transition to sustained growth.

Condensation sink (CS) emerged as a key limiting factor for nucleation, with intense NPF events consistently associated with lower early-morning CS values. Growth rates at CMN were typically higher than at JFJ, especially during summer, highlighting more favorable conditions for particle survival and growth. While background concentrations of small ions and particles were higher at JFJ, they did not translate into higher nucleation or growth efficiency, indicating that ion-induced nucleation alone is insufficient to sustain NPF in the absence of favorable thermodynamic and chemical conditions.

Cloud conditions, inferred from relative humidity thresholds (RH > 97%), significantly altered the observed size distributions, particularly suppressing particles in the CCN size range and introducing anomalous sub-10 nm modes. Ion concentrations, particularly positive cluster ions, were strongly reduced under in-cloud conditions, consistent with efficient ion scavenging.

In conclusion, mountain observatories, even within the same continental region, can exhibit markedly different aerosol dynamics due to differences in atmospheric coupling, precursor availability, and altitude. CMN is characterized by higher variability of aerosol populations and stronger coupling with regional sources, while JFJ serves as a more pristine reference point for background FT conditions. These results highlight the need for long-term, harmonized observations of ions and ultrafine particles to improve parameterizations of NPF in chemical transport and climate models, particularly in regions where the FT is intermittently influenced by boundary layer intrusions.

Acknowledgements. This work was carried out in the framework of EU/ESFRI ACTRIS Research Infrastructure (Aerosols, Clouds, and Trace gases Research InfraStructure). We received support from the Italian Ministry for University and Research (MUR) through PON PER-ACTRIS-IT (PNIR 2014-2020) and ITINERIS (EU – Next Generation EU PNRR- Mission 4. Component 2, Investment 3.1) projects. Martina Mazzini grant was funded by the project CIR01_00015_PER_ACTRIS_IT "Potenziamento della componente italiana della Infrastruttura di Ricerca ACTRIS – Rafforzamento del Capitale Umano". The authors gratefully acknowledge the Italian Air Force (CAMM) for access and logistic support at Mt. Cimone. The authors also thank Francescopiero Calzolari and Fabrizio Roccato for their technical support and data transfer at the Ottavio Vittori Observatory at Monte Cimone. We acknowledge the use of the Python package nais-processor by Janne Lampilahti, available at https://github.com/jlpl/nais-processor, for the analysis of NAIS data. We acknowledge the use of the Python package ranking-hy by Diego Aliaga, available at https://github.com/daliagachc/ranking-hy, for the analysis of NPF using the nanoparticle ranking method. The continuous aerosol measurements at the Jungfraujoch site are supported by MeteoSwiss in the framework of the Swiss

contributions (GAW-CH) to the Global Atmosphere Watch program of the World Meteorological Organization (WMO) and the ACTRIS research infrastructure funded by the Swiss State Secretariat for Education, Research and Innovation (SERI). We acknowledge the International Foundation High Altitude Research Stations Jungfraujoch and Gornergrat (HFSJG), 3012 Bern, Switzerland, which made it possible

420   for us to carry out measurements at the High Altitude Research Station at Jungfraujoch, with a special thanks to Claudine Frieden, Markus Leuenberger, and the custodians Christine and Ruedi Käser, and Daniela Bissig and Erich Furrer. The authors acknowledge the use of ChatGPT (OpenAI) to assist in editing the English language in the manuscript. All scientific content, interpretation, and analysis remain the sole responsibility of the authors.

References

425 Aliaga, D., Tuovinen, S., Zhang, T., Lampilahti, J., Li, X., Ahonen, L., Kokkonen, T., Nieminen, T., Hakala, S., Paasonen, P., et al.: Nano Ranking Analysis: determining NPF event occurrence and intensity based on the concentration spectrum of formed (sub-5 nm) particles, Aerosol Research Discussions, 2023, 1–19, 2023.

Bianchi, F., Tröstl, J., Junninen, H., Frege, C., Henne, S., Hoyle, C. R., Molteni, U., Herrmann, E., Adamov, A., Bukowiecki, N., et al.: New particle formation in the free troposphere: A question of chemistry and timing, Science, 352, 1109–1112, 2016.

430 Bianchi, F., Sinclair, V. A., Aliaga, D., Zha, Q., Scholz, W., Wu, C., Heikkinen, L., Modini, R., Partoll, E., Velarde, F., et al.: The SALTENA experiment: Comprehensive observations of aerosol sources, formation, and processes in the South American Andes, Bulletin of the American Meteorological Society, 103, E212–E229, 2022.

Boulon, J., Sellegri, K., Hervo, M., Picard, D., Pichon, J.-M., Fréville, P., and Laj, P.: Investigation of nucleation events vertical extent: a long term study at two different altitude sites, Atmospheric Chemistry and Physics, 11, 5625–5639, 2011.

435 Bousiotis, D., Brean, J., Pope, F. D., Dall'Osto, M., Querol, X., Alastuey, A., Perez, N., Petäjä, T., Massling, A., Nøjgaard, J. K., et al.: The effect of meteorological conditions and atmospheric composition in the occurrence and development of new particle formation (NPF) events in Europe, Atmospheric Chemistry and Physics, 21, 3345–3370, 2021.

Bukowiecki, N., Weingartner, E., Gysel, M., Coen, M. C., Zieger, P., Herrmann, E., Steinbacher, M., Ga, H. W., Baltensperger, U., et al.: A review of more than 20 years of aerosol observation at the high altitude research station Jungfraujoch, Switzerland (3580 m asl), Aerosol

440 and Air Quality Research, 16, 764–788, 2016.

Collaud Coen, M., Andrews, E., Aliaga, D., Andrade, M., Angelov, H., Bukowiecki, N., Ealo, M., Fialho, P., Flentje, H., Hallar, A., et al.: Identification of topographic features influencing aerosol observations at high altitude stations, Atmospheric Chemistry and Physics, 18, 12 289–12 313, 2018.

Cristofanelli, P., Brattich, E., Decesari, S., Landi, T. C., Maione, M., Putero, D., Tositti, L., and Bonasoni, P.: High-Mountain Atmospheric

445 Research: The Italian Mt. Cimone WMO/GAW Global Station (2165 M Asl), Springer, 2018.

Dada, L., Paasonen, P., Nieminen, T., Buenrostro Mazon, S., Kontkanen, J., Peräkylä, O., Lehtipalo, K., Hussein, T., Petäjä, T., Kerminen, V.-M., et al.: Long-term analysis of clear-sky new particle formation events and nonevents in Hyytiälä, Atmospheric Chemistry and Physics, 17, 6227–6241, 2017.

Dal Maso, M., Kulmala, M., Riipinen, I., Wagner, R., Hussein, T., Aalto, P. P., and Lehtinen, K. E.: Formation and growth of fresh atmospheric

450 aerosols: eight years of aerosol size distribution data from SMEAR II, Hyytiälä, Finland, Boreal environment research, 10, 323, 2005.

Dinoi, A., Gulli, D., Weinhold, K., Ammoscato, I., Calidonna, C. R., Wiedensohler, A., and Contini, D.: Characterization of ultrafine particles and the occurrence of new particle formation events in an urban and coastal site of the Mediterranean area, Atmospheric Chemistry and Physics, 23, 2167–2181, 2023.

Dunne, E. M., Gordon, H., Kürten, A., Almeida, J., Duplissy, J., Williamson, C., Ortega, I. K., Pringle, K. J., Adamov, A., Baltensperger, U.,

455 et al.: Global atmospheric particle formation from CERN CLOUD measurements, Science, 354, 1119–1124, 2016.

Foucart, B., Sellegri, K., Tulet, P., Rose, C., Metzger, J.-M., and Picard, D.: High occurrence of new particle formation events at the Maïdo high-altitude observatory (2150 m), Réunion (Indian Ocean), Atmospheric Chemistry and Physics, 18, 9243–9261, 2018.

Fuzzi, S., Baltensperger, U., Carslaw, K., Decesari, S., Denier van der Gon, H., Facchini, M. C., Fowler, D., Koren, I., Langford, B., Lohmann, U., et al.: Particulate matter, air quality and climate: lessons learned and future needs, Atmospheric chemistry and physics, 15, 8217–8299,

460 2015.

Herrmann, E., Weingartner, E., Henne, S., Vuilleumier, L., Bukowiecki, N., Steinbacher, M., Conen, F., Collaud Coen, M., Hammer, E., Jurányi, Z., et al.: Analysis of long-term aerosol size distribution data from Jungfraujoch with emphasis on free tropospheric conditions, cloud influence, and air mass transport, Journal of Geophysical Research: Atmospheres, 120, 9459–9480, 2015.

Hirsikko, A., Nieminen, T., Gagné, S., Lehtipalo, K., Manninen, H., Ehn, M., Hõrrak, U., Kerminen, V.-M., Laakso, L., McMurry, P., et al.: Atmospheric ions and nucleation: a review of observations, Atmospheric Chemistry and Physics, 11, 767–798, 2011.

Hussein, T., Dal Maso, M., Petäjä, T., Koponen, I. K., Paatero, P., Aalto, P. P., Hämeri, K., and Kulmala, M.: Evaluation of an automatic algorithm for fitting the particle number size distributions, Boreal environment research, 10, 337, 2005.

IPCC: Climate Change 2021: The Physical Science Basis, Cambridge University Press, Cambridge, United Kingdom and New York, NY, USA, https://www.ipcc.ch/report/ar6/wg1/, contribution of Working Group I to the Sixth Assessment Report of the Intergovernmental Panel on Climate Change, 2021.

Kangasluoma, J., Cai, R., Jiang, J., Deng, C., Stolzenburg, D., Ahonen, L. R., Chan, T., Fu, Y., Kim, C., Laurila, T. M., et al.: Overview of measurements and current instrumentation for 1–10 nm aerosol particle number size distributions, Journal of Aerosol Science, 148, 105 584, 2020.

Kerminen, V.-M., Chen, X., Vakkari, V., Petäjä, T., Kulmala, M., and Bianchi, F.: Atmospheric new particle formation and growth: review of field observations, Environmental Research Letters, 13, 103 003, 2018.

Kulmala, M., Lehtinen, K., and Laaksonen, A.: Cluster activation theory as an explanation of the linear dependence between formation rate of 3nm particles and sulphuric acid concentration, Atmospheric Chemistry and Physics, 6, 787–793, 2006.

Kulmala, M., Petäjä, T., Nieminen, T., Sipilä, M., Manninen, H. E., Lehtipalo, K., Dal Maso, M., Aalto, P. P., Junninen, H., Paasonen, P., et al.: Measurement of the nucleation of atmospheric aerosol particles, Nature protocols, 7, 1651–1667, 2012.

Laj, P., Bigi, A., Rose, C., Andrews, E., Lund Myhre, C., Collaud Coen, M., Wiedensohler, A., Schultz, M., Ogren, J. A., Fiebig, M., et al.: A global analysis of climate-relevant aerosol properties retrieved from the network of GAW near-surface observatories, Atmospheric Measurement Techniques Discussions, 2020, 1–70, 2020.

Lee, S.-H., Gordon, H., Yu, H., Lehtipalo, K., Haley, R., Li, Y., and Zhang, R.: New particle formation in the atmosphere: From molecular clusters to global climate, Journal of Geophysical Research: Atmospheres, 124, 7098–7146, 2019.

Lugauer, M., Baltensperger, U., Furger, M., Gäggeler, H., Jost, D., Nyeki, S., and Schwikowski, M.: Influences of vertical transport and scavenging on aerosol particle surface area and radon decay product concentrations at the Jungfraujoch (3454 m above sea level), Journal of Geophysical Research: Atmospheres, 105, 19 869–19 879, 2000.

Manninen, H. E., Petäjä, T., Asmi, E., Riipinen, I., Nieminen, T., MikkiIä, J., Hõrrak, U., Mirme, A., Mirme, S., Laakso, L., et al.: Long-term field measurements of charged and neutral clusters using Neutral cluster and Air Ion Spectrometer (NAIS)., Boreal Environment Research, 14, 2009.

Marinoni, A., Cristofanelli, P., Calzolari, F., Roccato, F., Bonafè, U., and Bonasoni, P.: Continuous measurements of aerosol physical parameters at the Mt. Cimone GAW Station (2165 m asl, Italy), Science of the total environment, 391, 241–251, 2008.

Merikanto, J., Spracklen, D., Mann, G., Pickering, S., and Carslaw, K.: Impact of nucleation on global CCN, Atmospheric Chemistry and Physics, 9, 8601–8616, 2009.

Nieminen, T., Kerminen, V.-M., Petäjä, T., Aalto, P. P., Arshinov, M., Asmi, E., Baltensperger, U., Beddows, D. C., Beukes, J. P., Collins, D., et al.: Global analysis of continental boundary layer new particle formation based on long-term measurements, Atmospheric Chemistry and Physics, 18, 14 737–14 756, 2018.

Peng, J., Hu, M., Wang, Z., Huang, X., Kumar, P., Wu, Z., Guo, S., Yue, D., Shang, D., Zheng, Z., et al.: Submicron aerosols at thirteen diversified sites in China: size distribution, new particle formation and corresponding contribution to cloud condensation nuclei production, Atmospheric Chemistry and Physics, 14, 10 249–10 265, 2014.

Rinaldi, M., Gilardoni, S., Paglione, M., Sandrini, S., Fuzzi, S., Massoli, P., Bonasoni, P., Cristofanelli, P., Marinoni, A., Poluzzi, V., et al.: Organic aerosol evolution and transport observed at Mt. Cimone (2165 m asl), Italy, during the PEGASOS campaign, Atmospheric Chemistry and Physics, 15, 11 327–11 340, 2015.

Rose, C., Zha, Q., Dada, L., Yan, C., Lehtipalo, K., Junninen, H., Mazon, S. B., Jokinen, T., Sarnela, N., Sipilä, M., et al.: Observations of biogenic ion-induced cluster formation in the atmosphere, Science advances, 4, eaar5218, 2018.

Rose, C., Collaud Coen, M., Andrews, E., Lin, Y., Bossert, I., Lund Myhre, C., Tuch, T., Wiedensohler, A., Fiebig, M., Aalto, P., et al.: Seasonality of the particle number concentration and size distribution: a global analysis retrieved from the network of Global Atmosphere Watch (GAW) near-surface observatories, Atmospheric Chemistry and Physics Discussions, 2021, 1–69, 2021.

Rosenfeld, D., Andreae, M. O., Asmi, A., Chin, M., de Leeuw, G., Donovan, D. P., Kahn, R., Kinne, S., Kivekäs, N., Kulmala, M., et al.: Global observations of aerosol-cloud-precipitation-climate interactions, Reviews of Geophysics, 52, 750–808, 2014.

Seinfeld, J. H., Bretherton, C., Carslaw, K. S., Coe, H., DeMott, P. J., Dunlea, E. J., Feingold, G., Ghan, S., Guenther, A. B., Kahn, R., et al.: Improving our fundamental understanding of the role of aerosol- cloud interactions in the climate system, Proceedings of the National Academy of Sciences, 113, 5781–5790, 2016.

Sellegri, K., Rose, C., Marinoni, A., Lupi, A., Wiedensohler, A., Andrade, M., Bonasoni, P., and Laj, P.: New particle formation: A review of ground-based observations at mountain research stations, Atmosphere, 10, 493, 2019.

Tröstl, J., Herrmann, E., Frege, C., Bianchi, F., Molteni, U., Bukowiecki, N., Hoyle, C. R., Steinbacher, M., Weingartner, E., Dommen, J., et al.: Contribution of new particle formation to the total aerosol concentration at the high-altitude site Jungfraujoch (3580 m asl, Switzerland), Journal of Geophysical Research: Atmospheres, 121, 11–692, 2016.

Venzac, H., Sellegri, K., and Laj, P.: Nucleation events detected at the high altitude site of the Puy de Dôme Research Station, France., Boreal environment research, 12, 2007.

Venzac, H., Sellegri, K., Laj, P., Villani, P., Bonasoni, P., Marinoni, A., Cristofanelli, P., Calzolari, F., Fuzzi, S., Decesari, S., et al.: High frequency new particle formation in the Himalayas, Proceedings of the National Academy of Sciences, 105, 15 666–15 671, 2008.

Vitali, B., Bettineschi, M., Cholakian, A., Zardi, D., Bianchi, F., Sinclair, V. A., Mikkola, J., Cristofanelli, P., Marinoni, A., Mazzini, M., Heikkinen, L., Aurela, M., Paglione, M., Bessagnet, B., Tuccella, P., and Ciarelli, G.: Analysis of chemical and transport processes of biogenic aerosols over the northern Apennines: insights from the WRF-CHIMERE model, Environmental Science: Atmospheres, 4, 967–987, https://doi.org/10.1039/D4EA00040D, 2024.

Wagner, R., Yan, C., Lehtipalo, K., Duplissy, J., Nieminen, T., Kangasluoma, J., Ahonen, L. R., Dada, L., Kontkanen, J., Manninen, H. E., et al.: The role of ions in new particle formation in the CLOUD chamber, Atmospheric Chemistry and Physics, 17, 15 181–15 197, 2017.

WHO: Review of evidence on health aspects of air pollution: REVIHAAP project: technical report, Tech. rep., World Health Organization. Regional Office for Europe, 2021.

Wiedensohler, A., Birmili, W., Nowak, A., Sonntag, A., Weinhold, K., Merkel, M., Wehner, B., Tuch, T., Pfeifer, S., Fiebig, M., et al.: Mobility particle size spectrometers: harmonization of technical standards and data structure to facilitate high quality long-term observations of atmospheric particle number size distributions, Atmospheric Measurement Techniques, 5, 657–685, 2012.

Zhao, B., Donahue, N. M., Zhang, K., Mao, L., Shrivastava, M., Ma, P.-L., Shen, J., Wang, S., Sun, J., Gordon, H., Tang, S., Fast, J., Wang, M., Gao, Y., Yan, C., Singh, B., Li, Z., Huang, L., Lou, S., Lin, G., Wang, H., Jiang, J., Ding, A., Nie, W., Qi, X., Chi, X., and Wang, L.:

Global variability in atmospheric new particle formation mechanisms, Nature, 631, 98–105, https://doi.org/10.1038/s41586-024-07547-1, publisher: Nature Publishing Group, 2024.